DRAFT

A Collimated Retarding Potential Analyzer for the Study of Magnetoplasma Rocket Plumes

T. W. Glover, A. A. Chan, and F. R. Chang-Diaz
Department of Physics and Astronomy, Rice University, Houston, Texas 77005

C. Kittrell
Chemistry Department, Rice University, Houston, Texas 77005

A gridded retarding potential analyzer (RPA) has been developed to characterize the magnetized plasma exhaust of the 10 kW Variable Specific Impulse Magnetoplasma Rocket (VX-10) experiment at NASA's Advanced Space Propulsion Laboratory. In this system, plasma is energized through coupling of radio frequency waves at the ion cyclotron resonance (ICR). The particles are subsequently accelerated in a magnetic nozzle to provide thrust. Downstream of the nozzle, the RPA's mounting assembly enables the detector to make complete axial and radial scans of the plasma. A multichannel collimator can be inserted into the RPA to remove ions with pitch angles greater than ~1°. A calculation of the general collimator transmission as a function over velocity space is presented, which shows the instrument's sensitivity in detecting changes in both the parallel and perpendicular components of the ion energy. Data from initial VX-10 ICRH experiments show evidence of ion heating.
52.70.-m

I. INTRODUCTION

The experiment motivating the development of this RPA is a 10 kW laboratory prototype of the Variable Specific Impulse Magnetoplasma Rocket (VASIMR) engine designated as VX-10[1]. This two-stage thruster consists of a helicon plasma source[2,3] first stage and a second stage RF "booster" antenna that can be used as an ion cyclotron resonant heating (ICRH) system. The axial profile of the VX-10 magnetic field is shown in Figure 1. The plasma is created in the weak field region of the helicon first stage and pumped through the high magnetic throat by an ambipolar electric field. Power addition at the RF booster occurs just downstream of the throat. The expanding field produces a magnetic nozzle that converts energy from the perpendicular motion of the particles into axial energy and hence rocket thrust.

The plasma diagnostics used in the VX-10 are very similar to those used in fusion experiments, but adapted to meet the high-speed flow conditions of the plasma jet. The RPA was primarily developed to examine the plasma in the exhaust section of the engine, and thereby explore the physical processes taking place in the plasma both with and without the application of additional RF power via the booster stage. By modeling the response of the collimated retarding potential analyzer (RPA) to both the parallel and perpendicular components of the exhaust plume ion velocity distribution, we demonstrate the utility of such a device as a diagnostic probe.

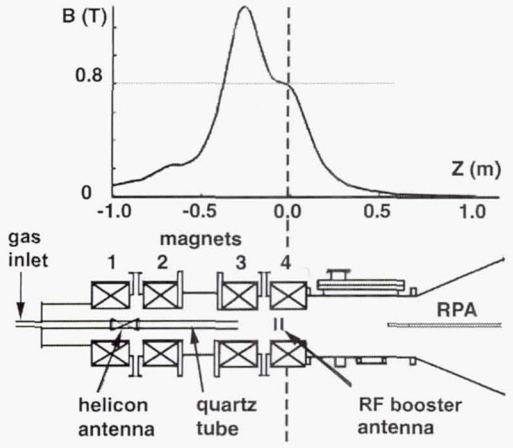

Figure 1: Typical magnetic field profile for ion cyclotron heating experiments.

The remainder of this paper is divided into four main sections. In Sec. II we describe the parameters of the VX-10 experiment that were factors in the design of the RPA. In Sec. III, we briefly describe construction techniques and similarities to previous analyzer designs. Section IV is a detailed calculation of the collimator transmission characteristics. This calculation is essential in using the collimated RPA as a perpendicular energy diagnostic. In Sec. V we present initial ion cyclotron heating experimental

data illustrating the sensitivity of this technique in practice.

II. VX-10 MAGNETIC FIELD AND PLASMA

A simplified schematic of the VX-10 architecture is shown in Figure 2. A conical adapter connects the VX-10 device on the left to a 5 m^3 vacuum chamber on the right, in which the RPA's support structure is mounted. As we shall describe later, the probe is able to axially and radially scan most of the exhaust plume. Moreover, by entering the rocket's exhaust from downstream, the axial probe shaft intercepts less of the plume than a radially mounted probe, thereby minimizing the perturbations to the flow and electrostatic potential field in the plasma.

In a typical experiment with helium propellant, the amplifier for the downstream antenna is fixed in frequency at approximately 3 MHz so the fundamental cyclotron resonance condition is established where the magnetic field is 0.8 T, indicated by the light horizontal line in the field strength plot of Figure 1. While the resonance condition is also met at a second point upstream of the magnetic throat, the RF waves are suppressed there by an RF baffle that has been integrated into the experiment for this purpose.

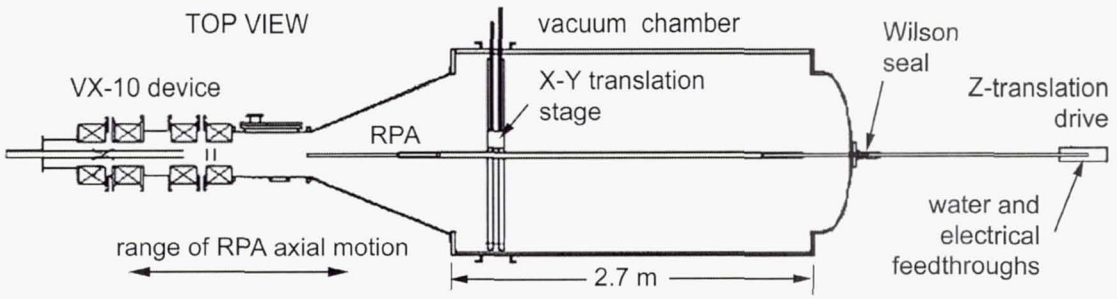

Figure 2: The RPA (Retarding Potential Analyzer) energy analyzer is mounted on a 6-m boom that enters the vacuum chamber through the Wilson seal shown at right. Z (axial) translation is accomplished with a manual drive that advances the probe shaft along a linear gear. Motion in the X (horizontal, perpendicular to the machine axis) and Y (vertical) directions is accomplished by the X-Y translation stage, which can bring the probe to the chamber walls upstream of the conical section.

In contrast to a magnetic-mirror confinement device, the VX-10 has only one region of strong magnetic field. This choke, produced by magnet 3, is located at the downstream end of the quartz tube that confines the helicon plasma. The helicon plasma is therefore bounded on its upstream end by a high-pressure gas cushion at the inlet and on its downstream side by the magnetic choke. In further contrast to fusion experiments, ion heating is applied on the downstream side of the choke, typically at the plateau in field strength between magnets 3 and 4 so that the energized ions are accelerated away from the source by the magnetic field gradient. The expanding field downstream of magnet 4 acts as a magnetic nozzle, converting the perpendicular energy imparted by ICRH to axial energy, resulting in thrust. In this region, where most of the RPA data is taken, plasma density is typically 10^{11} cm^{-3} on-axis and the electron temperature is typically 5 eV[4].

The amount of energy given to the ions is a variable[5], which can be tuned to operational requirements imposed by the propulsion system. The immediate experimental goal is to impart approximately 100 eV to the ions' perpendicular energy at the resonance near the antenna. This perpendicular energy is to be converted to parallel energy by the magnetic nozzle.

In addition to ion cyclotron heating, a second mechanism contributes to the plasma acceleration. This is the ambipolar electric field whose characteristics are largely determined by the electron temperature, the boundary conditions within the helicon source, and the magnetic field structure. Using helium, with a peak magnetic field of 1.5 T and an electron temperature in the exhaust of 5 eV, we observe ambipolar ion energies up to 60 eV. Similar results in argon have been recently observed by Cohen et al.[6]

III. ANALYZER DESIGN

Our design for the basic detector follows the principles described by Molvik[7] for the RPAs used to measure end-loss ions from the TMX and 2XIIB mirror machines at Lawrence Livermore National Laboratory (LLNL). However, the present system adds several features to the basic design that are specially tailored to the requirements of the VX-10. A primary requirement is smaller probe size. The RPA's in the Livermore 2XIIB experiment were 5 cm and 30 cm in diameter. The plasma in much of the VX-10 exhaust region is on the order of 10 cm in diameter, much smaller than the plasma sampled by the TMX RPAs. The VX-10 RPA was therefore designed to fit into a housing whose outer diameter is just under 2 cm to keep the probe diameter significantly smaller than the plasma diameter. Besides smaller size, requirements for the VX-10 probe were: instrument mobility within the chamber, durability under the thermal load of the rocket exhaust, and, most importantly, sensitivity to changes in both the perpendicular and parallel components of the ion energy. These will now be taken up sequentially.

A. Instrument Mobility

The magnetic field of the nozzle drops from its peak strength near the bore of magnet 3 to less than 1% of the peak over a distance of about 1 m (see Figure 1). Measurements throughout this axial range and over tens of centimeters in the radial direction are desired to map the two-dimensional acceleration processes in the exhaust plume. To achieve these objectives, and in contrast to the axially-fixed TMX RPAs, our instrument is mounted on a 6-m boom that permits 1.5 m of axial travel with up to 30 cm radial offset. As shown in Figure 2, the detector face can scan within a cylindrical volume encompassing the expansion region of the magnetic nozzle, from a point midway between magnets 2 and 3 to a point 1 m downstream from magnet 4. The boom rests on a translation stage that allows the detector to be moved perpendicular to the axis, both horizontally and vertically. The central section of the boom consists of a 3 m long, 3.8 cm diameter thin-walled stainless steel tube, vented to the chamber by a number of holes along its length. A 2.44 m aft section of 1.9 cm diameter pipe telescopes from the rear. This aft section passes through a Wilson seal on the rear wall of the vacuum chamber and carries cooling water and wiring to vacuum feedthroughs. A 90 cm length of 1.9 cm diameter stainless steel pipe extends from the forward end of the 3 m tube to support the 1.9 cm diameter copper housing for the RPA's internal components.

Figure 3 is a schematic showing the arrangement of the internal components. The grids and collector can be biased to examine either ion or electron energy spectra. Hence, the first grid in Figure 3 is labelled simply 'repeller' as its function is the same in either ion or electron mode: to repel the species not being measured. For radial scanning of the plasma, the collimator is replaced by a 2.5 mm diameter aperture. At radial positions up to 20 cm from the center of the plasma, the angle between the axis of the detector and the axis of the chamber is less than 2.5° due to the length of the boom. However, even this small angle is enough to reduce the collimated current to zero so collimated measurements are restricted to the experiment axis. With the aperture in place, ions with pitch angles of up to approximately 30° (depending on axial probe position and magnetic field profile) are accepted to the detector, so that the 2.5° variation in alignment in a radial scan has little effect on the instrument response.

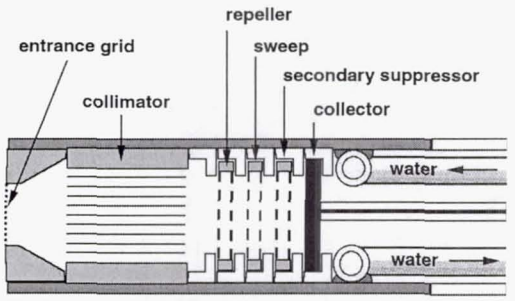

Figure 3: Energy analyzer internal configuration with collimator. The diameter of the plasma beam passing through the collimator is set by the diameter of the entrance grid. Ions entering the collimator with pitch angles greater than approximately 1° are not transmitted.

B. Grid Design

Following Molvik's guidelines[4], the entrance grids are designed to attenuate the incident plasma to a density low enough to: 1) ensure that the Debye length at the first voltage-bearing grid is larger than the grids' wire spacing, 2) reduce the thermal load on the delicate internal grids to

tolerable levels and 3) minimize space-charge effects on the electric fields between the grids. A simple criterion for limiting the space-charge effects derived by T. S. Green[8] was used in selecting the entrance grid transmission. Typical entrance grid material (see left panel of Figure 4) is 0.015" thick perforated steel, with a transmission of 1% and front surface hole diameter 0.025 cm. The holes are conical, with their larger diameters on the downstream side of the grid to allow transmission of ions over a wide range of angle of incidence. A 1.3 cm diameter disk of this material is silver-soldered to a 10 gram copper body that is in firm contact with the cooled copper housing described below in the section covering thermal load management.

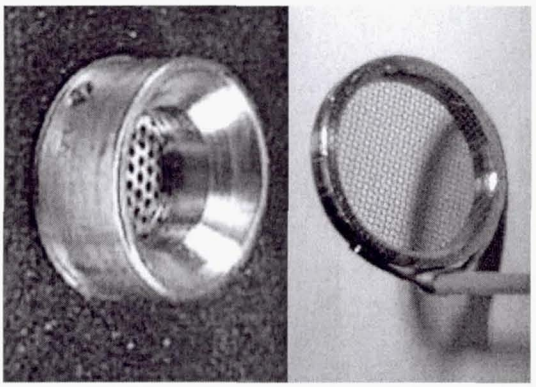

Figure 4: (*left*) A 1% transmission entrance grid in heavy copper mount (diameter 1.71 cm, mass 10 g) attenuates the incident plasma density to raise the internal Debye length. The entrance grid holes are conical, with the larger diameter hole openings on the downstream side visible in the photo. *(right)* High transmission (0.82^2) internal grid (diameter 1.27 cm) with wire spacing of 300 μm, less than the typical internal Debye length.

The mesh of the internal grids (right panel of Figure 4) has a transmission of 82% with a wire spacing of 300 microns. Each internal grid is made by spot-welding the mesh to each side of a 1.5 mm long slice of 1.27 cm diameter stainless steel tubing, forming a cylindrical volume whose thickness is five times the wire spacing of the mesh. The doubled grids are held in Teflon supports. These supports have a diameter slightly less than the I.D. of the copper housing, allowing the internal components to be easily installed or removed. Pin and socket electrical connections are made approximately 20 cm behind the collector.

While there is a voltage dip in the center of each cell in the mesh, relative to the voltage applied to the grid, this defect drops off in the axial direction towards the center of the doubled grid volume with a scale length approximately that of the wire spacing. A doubled grid formed by two grids at the same potential separated by a gap several times the mesh cell size therefore establishes a central region of uniform potential equal to that applied to the grids. This ensures that all ions passing through such a doubled grid surmount precisely the same potential in their transits, despite the fact that they encounter slightly different potentials in the plane of the mesh. This solution to the voltage variation inherent in a mesh of finite wire spacing is described by Stephanakis and Bennett[9]; it essentially removes the effect of the spatial variation in the sweep grid voltage due to the voltage dip in the center of each mesh cell, improving the accuracy of the I-V characteristic over that of single-layer grids.

C. Thermal Load Management

The heavy copper construction of the entrance grid mounts is intended to meet the second requirement of the entrance grids, which is to reduce the thermal load on the delicate internal grids to tolerable levels. While the experiment is operated in pulsed mode at present, it is anticipated that with an upgrade of the vacuum pumping system, continuous discharge experiments at pressures low enough to simulate space conditions will be possible. While fusion experiments typically produce shots of plasma that last a few hundred milliseconds, the VX-10 can operate continuously. This means that the RPA has to be actively cooled to survive the continuous heat load from the plasma. In practice to date, the RPA has operated in the plasma for as long as 15 minutes of continuous discharge. Estimated plasma parameters at the RPA face for such a discharge are: electron density of 4×10^{11} cm^{-3}, electron temperature of 6 eV, ion drift velocities of 20 kilometers per second and ion temperature of 5 eV. We estimate the heat load to the RPA face with the following relations from Stangeby[10]. The electron heat flux across the sheath to a solid surface in a plasma is

$$q_{ss}^{e} = 2kT_e\Gamma_{se}$$
$$= 2kT_e(\tfrac{1}{4}n_{se}e^{eV_w/kT_e}\bar{c}_e)$$

where k is Boltzmann's constant, T_e is electron temperature, subscript *ss* stands for solid surface, subscript *se* stands for sheath edge, Γ is particle flux, n is particle density, V_W is the wall voltage relative to the plasma, and c_e is electron thermal speed. An estimate for the ion heat flux based on a drifting Maxwellian distribution is

$$q^{i,drft\ Max} = (\tfrac{5}{2}kT_i + \tfrac{1}{2}m_i v_d^2)nv_d,$$

where v_d is the ion drift velocity, m_i is the ion mass, and T_i is the ion temperature. Using the estimated parameters above, we obtain a thermal load on the face of the detector of approximately 10 W. If this were deposited into the 10 g entrance grid mount (made mostly of copper) without active cooling, this component's temperature would rise at approximately 3°C/sec. At this rate, the temperature would be high enough to damage the adjacent Teflon grid supports in about one minute. To permit long-duration experiments, a set screw holds the entrance grid in firm contact with the copper housing (a 10 cm length of 1.9 cm copper pipe) which is in turn cooled by 4.7 mm O.D. copper water lines that run through the length of the boom (refer to Figure 3). The cooling line is shaped to a three-quarter loop whose outer diameter matches the inner diameter of the housing. For good thermal contact, the cooling loop is silver-soldered to the housing, at its downstream end. Since the first entrance grid has a transmission of 1%, it absorbs 99% of the potential heat load to the delicate internal grids and diverts it to the water stream via the 10 cm long copper housing. Measurements have verified the effectiveness of the cooling system. A thermocouple embedded in one of the 10 gram entrance grid mounts reached an equilibrium temperature of 110° C after five minutes of exposure to conditions as described above.

D. Collimator Construction

Stenzel[11] demonstrated the utility of a collimator in obtaining a measurement of the ion parallel velocity distribution free of the influence of the perpendicular velocity distribution. Stenzel used a 0.6 mm thick disk of glass microchannel plate as a collimator, with hole diameters of 14 microns, spaced 18 microns apart. This device was used in a non-magnetized argon plasma of density 10^9 cm^{-3} penetrated by a 70 eV ion beam. In Stenzel's words,

> "... a conventional gridded energy analyzer yields an erroneously large beam temperature for diverging beams. The directional analyzer avoids this error ... and gives a trustworthy temperature value."

One of the central goals of our research is to determine whether power from the RF booster antenna is deposited into the perpendicular component of the ion energy or the parallel component; therefore, a detector that has a strong response to changes in ion perpendicular energy is crucial to verifying the ion cyclotron heating mechanism in the VX-10 experiment. Furthermore, an analyzer that can obtain accurate and precise measurements of the parallel energy distribution free of divergence effects is highly desirable.

Due to the thermal load and high energy ion bombardment in the VX-10 plasma, a collimator of more rugged construction than Stenzel's is needed. Therefore the collimator was constructed by bundling together 91 stainless steel hypodermic needles (O.D. 1.3 mm, I.D. 0.86 mm) in a close-packed hexagonal array. The needles were assembled in a hexagonal hole machined in a 2 cm length of 1.7 cm diameter brass stock to hold them with a snug fit. After silver-soldering them in place, the needles were cut flush with the surface of the brass. A photograph of the collimator is shown in Figure 5.

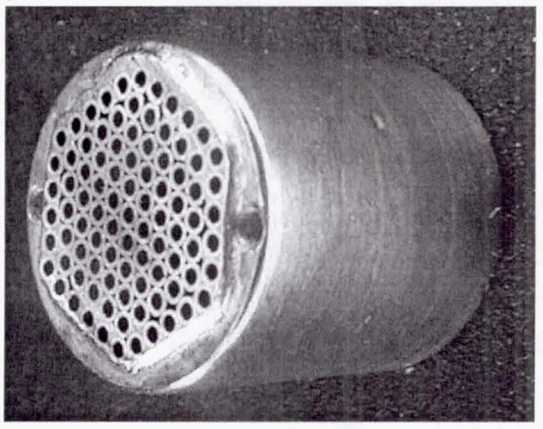

Figure 5: Collimator composed of stainless steel capillary tubes bundled into a close-packed hexagonal array; length = 2 cm, tube inner diameter = 0.86 mm; brass body diameter 1.7 cm.

IV. COLLIMATOR TRANSMISSION FUNCTION

A. Formulation of the Problem

The problem considered here is as follows: given the velocity distribution of charged particles entering a tube of length L and radius R in a magnetic field B, where the tube axis is parallel to B, what is the velocity distribution of the particles exiting the tube?

This problem has been considered previously. Krawec[12] performed theoretical and numerical calculations of the distortion of the axial velocity distribution of a Maxwellian plasma upon passage through a tube of arbitrary radius and length. Wang[13] calculated the transmission of electrons through a short tube of variable length as a function of ambient magnetic field. Wang's calculations compared favorably with experimental results, demonstrating that perpendicular electron energy can be measured in this way.

We have taken a somewhat different approach to this calculation, defining the transmission as a function of coordinates in velocity space. Calculating the transmission this way makes the collimator's restrictions on both gyroradius and pitch angle obvious, and provides a means of finding the distribution function of the outgoing particles for arbitrary input distributions. It also demonstrates clearly the collimator's sensitivity to elevation of the perpendicular component of the ion energy - the primary ion acceleration mechanism in the VX-10 concept.

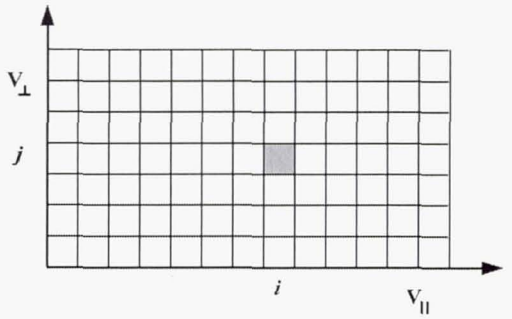

Figure 6: The transmission is calculated as a function of each point, or cell, in the $v_\perp$-$v_{//}$ velocity space. For the numerical calculation, the velocity domain is broken up into uniformly spaced values of $v_{//}$ (index label i) and uniformly spaced values of $v_\perp$ (index label j).

The velocity distribution is expressed as a function of the perpendicular and parallel velocity components, $v_\perp$ and $v_{//}$. We define the transmission function T as the ratio of the outgoing to the incoming distribution function, on a point-by-point basis in the velocity space, (illustrated in Figure 6):

$$T(v_{//i}, v_{\perp j}) \equiv \frac{f_{out}(v_{//i}, v_{\perp j})}{f_{in}(v_{//i}, v_{\perp j})} \qquad (1)$$

B. Particle Trajectories

Figure 7 illustrates the problem of calculating the value of T for a single point in the velocity space. Our point of view is looking into the tube from the exit, with the magnetic field coming out of the page. We refer to the particles as ions, keeping in mind that the calculation applies also to electrons. Note that r is the location of the particle's guiding center (GC), not the location of the particle itself.

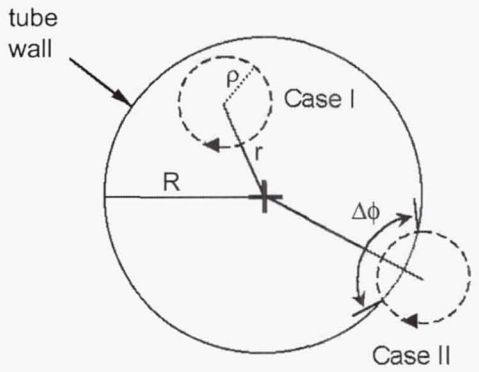

Figure 7: Ion trajectories as seen in projection from the exit of a single tube of the collimator. The tube axis is marked by the heavy cross. r is the distance from the tube axis to the guiding center of the ion trajectory and ρ is the gyroradius. $\Delta\phi$ is the angular size (as measured from the guiding center) of the portion of the Case II trajectory that is inside the tube wall.

In Case I, all particles are transmitted: T = 1. Inspection of Figure 7 makes clear that the condition for this case is

$$r + \rho < R, \qquad (2)$$

where the Larmor radius ρ is specified by the $v_\perp$ coordinate in velocity space, since

$$\rho = \frac{m\, v_\perp}{e\, B}. \qquad (3)$$

For this case, transmission is independent of $v_{//}$. (Note that since ρ also depends on m, the

transmission also depends on the particle species.)

In Case II, the transmission depends on $\Delta\phi$, the arc length of the portion of the trajectory that is inside the tube. $\Delta\phi$ in turn depends on ϕ, the phase, which specifies the orientation of $v_\perp$ as the ion crosses the entrance plane.

$\Delta\phi$ translates to a lower limit on $v_{//}$ in the following way. The particle must transit the length of the tube in a time less than or equal to the time needed to gyrate through $\Delta\phi$ the arc length between the ion position where it enters the tube and the tube wall. That is,

$$t_{transit} = \frac{L}{v_{//}} \leq \frac{\Delta\phi}{\omega} \tag{4}$$

where ω, the angular velocity, is given by

$$\omega = \frac{eB}{m} \tag{5}$$

so that we must have, for the ion to be transmitted,

$$v_{//} \geq \frac{eBL}{m\Delta\phi}. \tag{6}$$

Figures 8 and 9 illustrate how $\Delta\phi$ is calculated, given the radial location of a particle at the entrance of the tube, its gyroradius and the location of its guiding center. The location of the guiding center is determined once the direction of $v_\perp$ is specified by the phase angle ϕ measured relative to the x-axis (the horizontal line in Figures 8 and 9). We assume a uniform distribution in phase angle ϕ for the velocity vectors.

For both Figures 8 and 9,

$$\Psi_1 = cos^{-1}\left[\left(r^2 + \rho^2 - q^2\right)/2r\rho\right]$$
$$\Psi_2 = cos^{-1}\left[\left(r^2 + \rho^2 - R^2\right)/2r\rho\right] \tag{7}$$

Whether or not an ion is transmitted depends on the ion's radial location as it enters the tube (q), the orientation (ϕ) of the perpendicular component of its velocity, the magnitude of its perpendicular velocity ($v_\perp$), and its parallel velocity ($v_{//}$). We are concerned only with the dependence on the last two variables, so the final transmission we obtain will have the effects of the radial position q taken into account as a weighted average. The transmission is also averaged over phase angle ϕ by assuming a uniform distribution in ϕ for the incoming particles at the tube entrance and calculating the fraction transmitted for a given combination of the other variables.

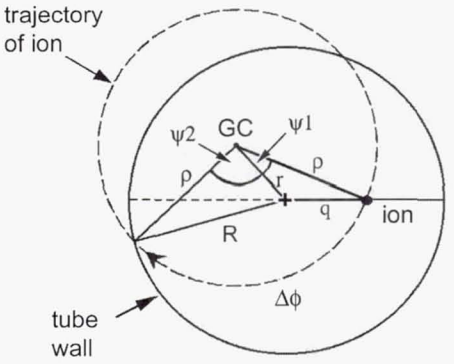

Figure 8: When the particle's guiding center is *above* the x-axis (horizontal dashed line), the amount of phase traversed before the particle hits the tube wall is $\Delta\phi = \psi1 + \psi2$.

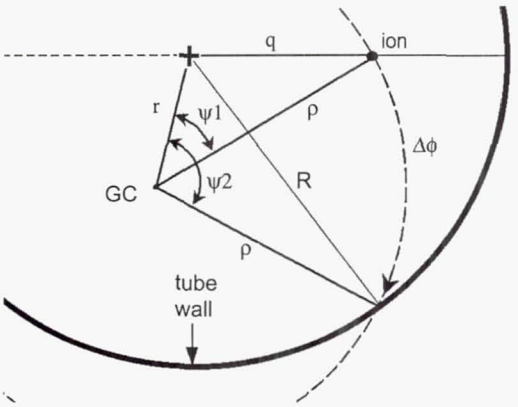

Figure 9: When the particle's guiding center is *below* the x-axis, the amount of phase traversed before the particle hits the tube wall is $\Delta\phi = \psi2 - \psi1$.

C. Accumulation of the Outgoing Distribution

Since the effective detector size is small relative to the dimensions of the plasma for the majority of the measurements, we assume that the velocity distribution is uniform across the entrance of the tube. As indicated above in equation 7, the transmission depends on the radial distance of the particle from the tube axis, so we begin the computation by breaking the cross-sectional area of the tube into annular sections (see Figure 10), where the mean radius

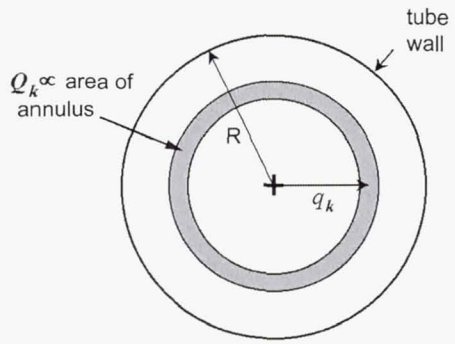

Figure 10: The transmission function for a given radius q_k is weighted by the ratio Q_k of the annular area to the tube cross-sectional area πR^2.

of an annulus is q_k and its width is Δq. The total number of particles which will be found at any radius is proportional to the area of the annulus so that we weight the value of the outgoing distribution at a given radius q_k by the factor

$$Q_k = \frac{\pi q_k^2 - \pi q_{k-1}^2}{\pi R^2} = \frac{(k\Delta q)^2 - [(k-1)\Delta q]^2}{R^2} \qquad 8)$$
$$= \left(\frac{\Delta q}{R}\right)^2 (2k-1)$$

Once the radial location q is specified, we set $v_\perp$ to its smallest value for the specified domain in velocity space (refer to Figure 6). With this combination of q and $v_\perp$, the velocity vector's orientation, specified by ϕ is stepped through 2π in uniform angular increments. For each value of ϕ, the location of the guiding center is found (Figure 11 illustrates the shift in the location of the guiding center as ϕ is incremented) and the ion's trajectory is tested by equation 2 to see if it intersects the tube wall.

If not (Case I), the value of the outgoing distribution function for all cells in the row of the velocity space with the current value of $v_\perp$ is incremented by

$$\Delta f_{out\_i,j,k,\phi} = \frac{Q_k}{N_\phi} \cdot f_{in}(v_{//i}, v_{\perp j}) \qquad (9)$$

that is, for all values of the parallel velocity index j. N_ϕ is the number of ϕ values into which 2π has been divided.

If the trajectory does intersect the wall (Case II), the minimum value of $v_{//}$ needed for the particle to pass through the tube is calculated from $\Delta\phi$ as indicated in equation 6. In contrast to Case I, only cells whose velocities are *above* this $v_{//}$ cutoff are incremented by the weighted value of equation 9.

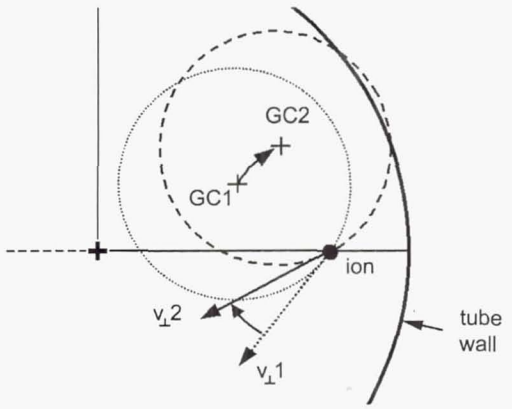

Figure 11: As the phase angle is incremented to rotate the perpendicular velocity vector, the guiding center moves to a new radial distance from the tube axis. The incremental movement shown here changes the calculation from Case I ($r + \rho < R$) to Case II ($r + \rho \geq R$).

Once ϕ has run through 2π, $v_\perp$ is incremented to its next cell value and the rotation of the velocity vector at the entrance through 2π is repeated. After this has been done for the last value of $v_\perp$ in the velocity space, we have the value of the outgoing distribution over the given domain in velocity space for the present radial location q_k. This result is added to the accumulated outgoing distribution function. The radial coordinate q is incremented and the calculation over the velocity space is repeated. The outgoing distribution is accumulated in this way until the increment from the last annular area element bounded by the tube radius is added to the total. The transmission is then calculated by dividing the value of each cell in the outgoing distribution by the corresponding value of the incoming distribution (taken as uniform for convenience). This algorithm has been implemented in MATLAB for use at ASPL.

D. Transmission Test Cases

We apply the following test cases to the transmission calculation. First, the transmission should be nearly 1 for all velocities for an aperture, which we may regard as a tube whose length is very short compared to its radius. In Figure 12, we see that the only particles blocked are those that have both low $v_{//}$ and high $v_\perp$, as

we would expect. As a check on the calculation, consider the transmission for ions with $v_{//} \approx 0$. At low parallel velocity, the only ions trans-

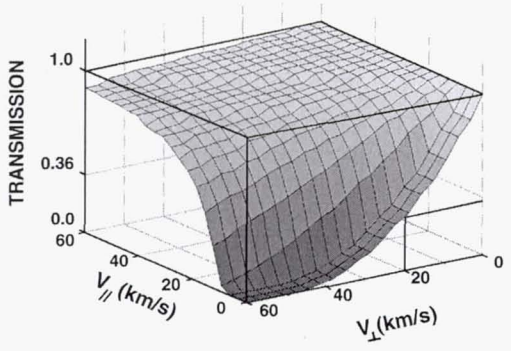

Figure 12: Orthogonal view of the collimator transmission function for an aperture, for H+ ions in a 0.1 T magnetic field. Tube radius R = 10 mm. Tube length L = 1 mm. Viewing angle chosen to reveal significant features of the transmission function; origin of coordinate system at right.

-mitted are those that execute full gyrations without hitting the tube wall. The transmission of such ions is zero outside a radius $q = R - 2\rho$, while the transmission of these ions inside this radius is one. Using this radius to calculate the area of transmission as a fraction of the total area, and using equation 3 to write ρ in terms of $v_\perp$, we obtain an expression for the transmission for small $v_{//}$,

$$T_{v_{//}\approx 0} = \left(1 - \frac{2mv_\perp}{eBR}\right)^2, \qquad (10)$$

that is valid up to $v_\perp = eBR/2m$, beyond which the transmission is zero. For the parameters of Figure 12, this limit is 48 km/s, in agreement with the plotted function. For $v_\perp$ = 20 km/s, equation 10 yields a transmission of 0.36, also in agreement with the calculated function and marked by a heavy line in Figure 12.

As the tube's ratio of length to radius is increased, we expect it to transmit fewer particles with high pitch angles. Figure 13 illustrates this effect for a tube with R = 1 mm and L = 2 mm. (Note the change in viewing angle from figure 12 to figure 13.)

Figure 13 illustrates two aspects of the transmission of a tube: 1) for low $v_{//}$, meaning so low that the ion executes a significant fraction of a gyration in traveling the length of the tube, the tube radius establishes a limit on $v_\perp$ and hence on the gyroradius. For $v_{//}$ higher than this limit, the tube transmission is governed mainly by the particle's pitch angle. Figure 14 shows the transmission of Figure 13 as a contour plot, the method of presentation we use for the

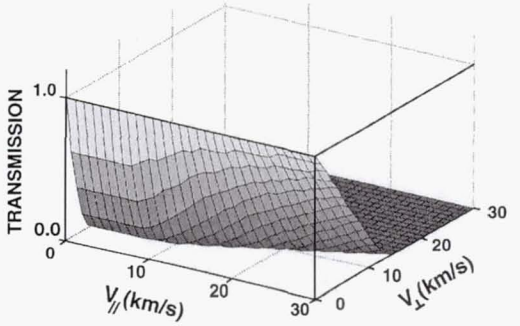

Figure 13: Transmission function of a short tube, for H+ ions in a 0.1 T magnetic field. Tube radius R = 1 mm. Tube length L = 2 mm. Viewing angle changed from that of Figure 12; origin of coordinate system at left.

transmission function from this point forward. Viewed in this way, we can see how the tube's transmission is a combination of a limit on gyroradius (proportional to $v_\perp$) and pitch angle $\theta = tan^{-1}(v_\perp/v_{//})$.

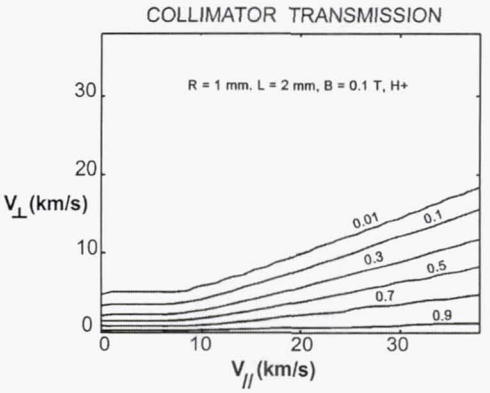

Figure 14: The transmission function of Figure 13, displayed as a contour plot in vertical projection; each contour line is labelled by the transmission value immediately above it.

As an additional test, we consider a collimator that consists of a cylinder capped by an entrance aperture. The only modification to the algorithm described above is to set the maximum value of q, the distance of the particle from the axis at the entrance, to the radius of the opening, which is

smaller than R, the radius of the cylinder. If the aperture's radius is small compared to that of the cylinder, the collimator has a sharp pitch angle limit equal to the half-angle of a cone with the radius and length of the cylindrical portion of the collimator. That is,

$$\theta_{max} = arctan\left(R/L\right) = arctan\left(v_{\perp}/v_{//}\right) \quad (11)$$

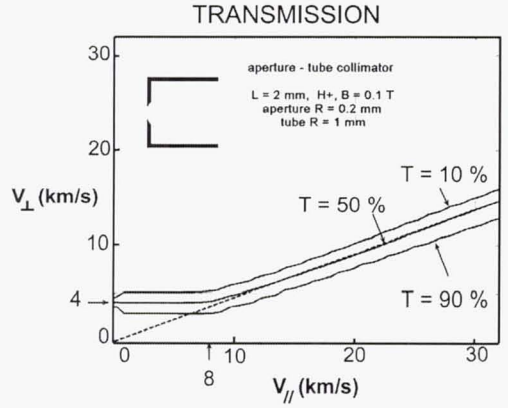

Figure 15: A collimator consisting of an open cylinder capped by an aperture at its entrance sets a limit to the pitch angle of transmitted ions, above a critical perpendicular velocity (here, 4 km/s) set by the cylinder and aperture radii. (Only the 10%, 50% and 90% transmission contours are shown.)

As the aperture radius approaches zero, T = 0 above the line in velocity space with slope *tan* θ and T = 1 below this line. For a finite radius aperture, the transmission makes a softer transition from 1 to 0 across the pitch angle limit and, for $v_{\perp}$ values less than that corresponding to a gyroradius equal to the tube radius, all particles are transmitted regardless of pitch angle since their trajectories can't reach the tube wall. Figure 15 illustrates these features.

The pitch-angle limit is valid only above the critical perpendicular velocity corresponding to the difference between the cylinder and aperture radii. That is, all ions entering the aperture with gyroradii less than half this difference are transmitted regardless of pitch angle. For the case illustrated in Figure 15, this perpendicular velocity cutoff is

$$v_{\perp C} = \frac{eB\rho}{m} = \frac{eB\left(R_C - R_A\right)}{m} = 7.7 \times 10^4 \, m/s \cdot \quad (12)$$

The lowest transmission shown in Figure 15 is the 10% contour, which lies at a slightly lower velocity. The contour plot also illustrates the soft edge of the transmission cutoff. Rather than zero transmission, a more meaningful transmission boundary might be the 50% contour, which lies considerably lower at about 4 km/s. Therefore, the parallel velocity above which the transmission is restricted by pitch angle rather than gyroradius (or $v_{\perp}$) is $v_{//} = v_{\perp C} \cdot L/R_{tube} \sim 8$ km/s.

With the test cases yielding transmissions in agreement with expectations, we now calculate the transmission of the collimator constructed for the RPA in the VX-10 experiment (photograph in Figure 5). Figure 16 is a contour plot of the transmission for singly ionized helium in a magnetic field whose strength matches that at the location of the RPA in measurements presented in a later section. The transmission function lies very close to the parallel velocity axis, so that the collimator essentially takes a slice through the velocity distribution along this axis. Note the difference in scale of the two velocity axes in Figure 16.

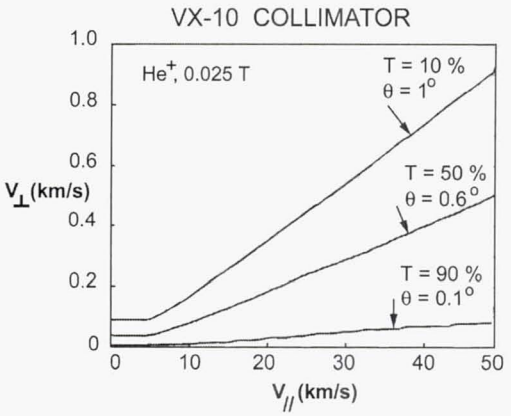

Figure 16: The transmission function of the energy analyzer's collimator for the magnetic field of the fundamental ICRF He+ heating experiments at Z = 55 cm. Note the different scales on the velocity axes. The majority of the ions passed by the collimator have velocity vectors within 1° of the axis.

The collimator alters the response of the RPA in two ways. First, by removing ions with pitch angles much above one degree, the resulting characteristic should be essentially that of a one-dimensional model with ion velocities parallel to the detector axis. Second, the sharp dropoff of the transmission with increasing pitch angle

means that a slight average increase in the ions' perpendicular energy – if not accompanied by other changes in the plasma parameters - will result in a distinct drop in the transmitted ion current. This is what makes the collimated RPA useful in evaluating the effectiveness of antennas designed to heat the plasma in the VX-10 experiment via the ion cyclotron resonance. To see this more clearly, Figure 17 shows the collimator transmission as a function of parallel and perpendicular kinetic energy rather than velocity. Plotted in energy space rather than velocity space, the region where the transmission is dominated by gyroradius contracts to insignificance due to the square in the mapping from velocity to energy; for plasmas with drift kinetic energies of 20 eV and ion temperatures of a few eV, typical of VX-10 experiments, the collimator is essentially a narrow pitch angle filter.

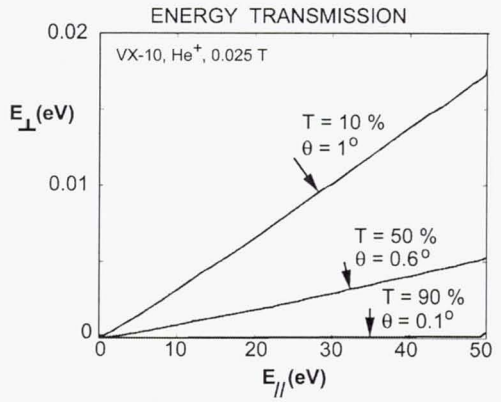

Figure 17: Transmission of the collimator at Z = 55 cm in the He+ fundamental ICRF magnetic field, as a function of parallel and perpendicular energy rather than velocity.

V. COLLIMATED RPA USE IN VX-10

The calculated transmission function described in the previous section has been used to compute simulated current-voltage characteristics for the collimated RPA; the simulated characteristics illustrate the changes to be expected with successful ion cyclotron heating. The software used to generate the characteristics includes the effect of a change in plasma potential which may accompany the application of power to the booster stage.

Arrow *a* in Figure 18 shows the shift of a simplified ion velocity distribution due to an increase in parallel energy such as that resulting from an increased plasma potential. This change in the plasma should produce a higher RPA saturation current in the characteristic in addition to the shift to higher parallel energy, since the ions' pitch angles are decreased by their higher parallel velocity, allowing more of them to pass through the collimator tubes. If the application of power to the plasma raises the ions' perpendicular energy (arrow *b*) in addition to the parallel energy boost from the higher plasma potential, the distribution can be moved into a region of velocity space where the collimator transmission is low enough to reduce the current.

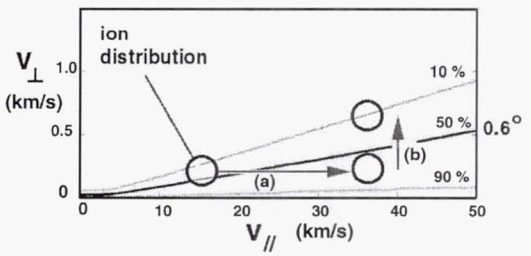

Figure 18: An increase in plasma potential (arrow *a*) shifts the ion distribution to the right, into a region of higher collimator transmission, resulting in higher current. Arrow *b* indicates the effect of added perpendicular energy sufficient to lower the current.

Figure 19 displays three simulated RPA characteristics illustrating the effects of the distribution changes of Figure 18. In these simulations, the ion velocity distribution in the 0.8 T resonance region is specified by a drift velocity and perpendicular and parallel temperatures. The software maps the input velocity distribution through the magnetic nozzle to the field strength at the RPA entrance and also takes into account the parallel acceleration due to the drop in electrostatic potential from the plasma potential in the resonance region to the grounded RPA entrance.

The calculation of a simulated characteristic begins by multiplying the incoming ion velocity distribution by the collimator transmission function to produce the transmitted velocity distribution. The transmitted distribution is then used to calculate the RPA current as a function of parallel energy by integrating over perpendicular velocity the number of ions for each value of parallel velocity, and converting each parallel velocity to the equivalent parallel energy. The energy distribution is then

calculated from the simulated characteristic in the same way as from experimental data:

$$f(E_{//}) \propto \frac{(dI/dV)}{\sqrt{V}} \qquad (13)$$

where V and I are sweep voltage and collected current respectively.

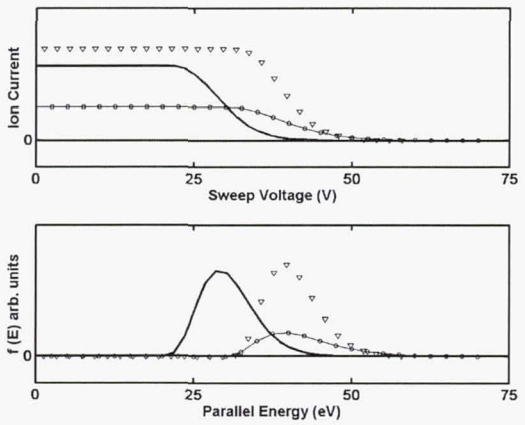

Figure 19: Simulated collimated RPA characteristics. Solid line: 20 km/s drift velocity, $T_{i//} = T_{i\perp} = 1$ eV, plasma potential = 20 V. Triangles: same velocity distribution, plasma potential increased to 30 V. Circles: 20 km/s drift velocity, $T_{i//} = T_{i\perp} = 2$ eV, plasma potential = 30 V.

The solid line in Figure 19 is the result of adjusting the simulation's input parameters of perpendicular and parallel ion temperature, drift velocity and plasma potential to obtain a characteristic that closely matches that obtained with the helicon plasma in the VX-10 experiment. The curve marked by triangles shows the effect of increasing the plasma potential at the resonance by 10 V, with the other parameters unchanged. This corresponds to the change marked as arrow *a* in Figure 18. The energy distribution is shifted 10 V to the right by the elevated plasma potential and the current increases due to the higher collimator transmission at lower pitch angles. The fine line marked with circles shows the effect of increasing the ion perpendicular (and parallel) temperature from 1 eV to 2 eV, corresponding to arrow *b* in Figure 18. The 10 V shift due to the increased plasma potential is the same as in the previous case, but the ion *current* in the characteristic drops significantly. This illustrates the ability of the collimated RPA to simultaneously indicate changes in both parallel and perpendicular components of the ion energy.

Figure 20 shows the experimental result of applying 3 kW of power to the RF booster antenna under *nonresonant* conditions. Here, the magnetic field under the antenna is 0.5 T rather than the 0.8 T required for ion cyclotron resonance at the RF booster frequency of 3 MHz. While there is a substantial increase in parallel

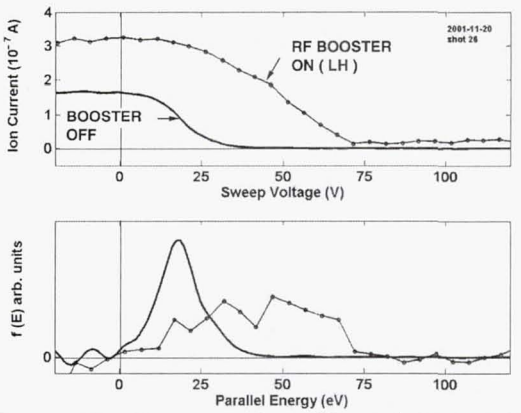

Figure 20: Upper panel: collimated RPA I-V characteristic for the helicon plasma (heavy line) and with 3 kW of left-hand polarized power applied to the RF booster antenna, *not* at the ion cyclotron frequency (fine line). Lower panel: parallel energy distributions, with and without the RF booster, derived from the RPA characteristic.

energy evident in the plot of the energy distribution (lower panel), the higher current in the I-V characteristic (upper panel) implies reduced ion pitch angles. While this does not preclude perpendicular heating, the amount is negligible compared to the increase in parallel energy.

Figure 21 shows the experimental result when the magnetic field under the antenna is increased to the 0.8 T required to put the ions' gyrofrequency at 3 MHz as they pass under the antenna, matching the frequency of the RF power. Compared with the nonresonant field experiment of Figure 21, there is still a parallel energy increase with power applied to the booster antenna, but the ion saturation current is *reduced* by the addition of booster power rather than raised as in Figure 20.

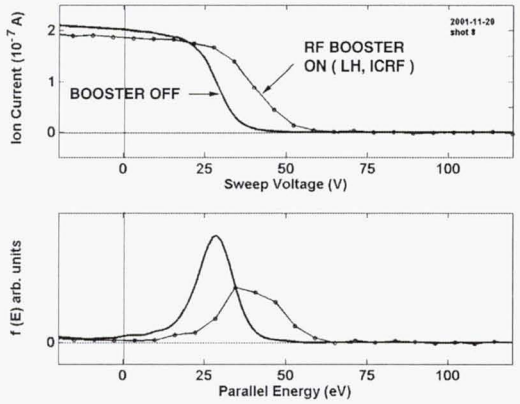

Figure 21: The collimated RPA current drops when power is applied to the RF booster at the ion cyclotron frequency.

When this experiment was repeated with the 2.5 mm aperture replacing the collimator in the RPA, the saturation current was observed to rise by approximately 50 % when power was applied to the booster. With the collimator removed, this increase in current indicates higher plasma density since the uncollimated RPA is relatively insensitive to pitch angle as discussed earlier. Emissive probe measurements show that the plasma potential increase is smaller for this magnetic field (0.8 T under the booster antenna) compared to the weaker field case (0.5 T under the antenna), in agreement with the smaller increase in parallel energy shown by the RPA. Observing that the plasma potential and density both increase when power is applied to the booster for both magnetic field cases, we can conclude with some confidence that the *decreased* collimated RPA current in the resonant field case is evidence of elevated ion perpendicular energy, as illustrated by the simulated collimated RPA characteristics. That this effect occurs only when the ion cyclotron resonance is near the booster antenna strongly suggests that ICRH is the mechanism responsible for the increased perpendicular energy.

These preliminary experiments were not expected to produce substantial ion heating because both the diameter and density of the plasma as it passed through the booster antenna were too low for effective antenna loading. The outcome of these experiments was that higher ion parallel energy was observed in the downstream exhaust region when power was applied to the booster, but this energy could be completely explained by the abrupt increase in plasma potential (as measured by a swept emissive probe) that accompanied the application of booster power. Nonetheless, distinct results – the reduced collimated RPA current - indicative of elevated perpendicular ion energy were obtained when the magnetic field strength at the ICRF antenna matched that required for the ion cyclotron resonance.

In comparing the experimental data of Figure 21 with the simulated characteristics in Figure 19, it would appear that the perpendicular energy imparted to the ions by the ion cyclotron mechanism was less than an electron volt. However, the presence of an appreciable neutral background pressure suggests that the ion heating may have been significantly higher, as follows.

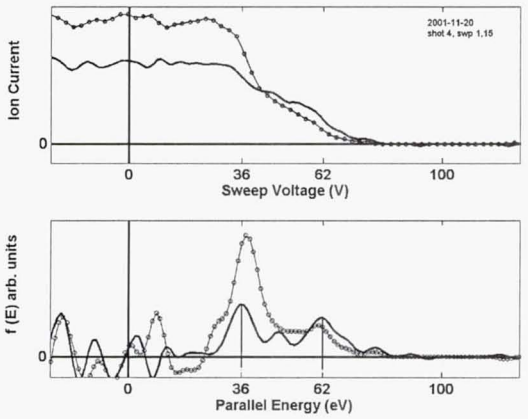

Figure 22: Upper panel: collimated RPA I-V characteristic for first (heavy line) and last (circles) sweeps of a 15-sweep set spanning the time interval from 0.4 seconds into the discharge to 0.8 seconds.

Collimated RPA data taken during the first second of the helicon discharge reveal an interesting evolution of the ion parallel energy distribution. Figure 22 shows the current-voltage characteristics and the corresponding parallel energy distributions at two times during a plasma shot: 0.4 seconds (heavy line) and 0.8 seconds (circles) after discharge initiation. Inspection of the 13 sweeps between the two shown makes it clear that the bimodal distribution is a real feature while the other peaks in the distribution are artifacts caused by temporal fluctuations in the ion current on a time scale short compared to the sweep period of 12.5 milliseconds. The lower energy side of the 36 eV peak corresponds to the plasma potential at the location of the RPA entrance as measured by

a swept emissive probe. Furthermore, the number of ions under the lower energy peak is directly proportional to the background neutral pressure at the location of the RPA entrance, which rises from 1.7 to 2.2 x 10^{-4} Torr in the time between the two RPA sweeps shown. These two observations suggest that the lower peak is due to ionization of the local background gas in the downstream section of the chamber where the RPA is located[14]. We therefore posit that only the ions in the 62 eV high energy peak have their origin in the helicon source. Similar pressure effects have been observed in other plasmas flowing in divergent magnetic fields[15].

In the VX-10 ion cyclotron heating experiments described in this paper, power was applied to the RF booster antenna when the ion population entering the RPA was dominated by the locally-generated, low energy component. This factor was not appreciated at the time of the experiments. Since these ions form some distance downstream from the ICRF fundamental resonance, they will not acquire perpendicular energy via this mechanism. If the picture of a locally generated plasma dominating the RPA signal under these conditions is correct, the total RPA current has two components: the high energy ions coming directly from the source upstream and the low energy ions formed by ionization of neutral gas downstream. The drop in current is due to the reduction in transmission of the relatively small number of ions in the high energy component, due to perpendicular heating under the booster antenna. With these complications, it is not possible to assess the amount of perpendicular energy imparted to the ions under the antenna. Simulation studies indicate that a perpendicular energy boost of approximately 10 eV is needed to reduce the current from the high energy component to negligible levels. If the reduction in current corresponds to the complete disappearance of the high energy component, then the figure of 10 eV is a lower bound on the heating achieved to date.

Improvements to the VX-10 device should allow the collimated RPA to make accurate estimates of the amount of ion cyclotron heating in future experiments. The background neutral pressure has been reduced substantially, not by additional pumping but by introducing a constriction at the exit of the quartz tube to reduce the tube's neutral flow conductance. With this modification, the helicon source now approaches 100 % ionization so that lower gas flow rates are sufficient to produce plasma of the density required for ICRH experiments. The lower flow rates in turn keep the background neutral pressure at significantly lower values during the discharge. Over the past year, the VX-10 helicon source has also been enlarged and optimized to provide a denser and larger diameter target plasma that should improve the booster antenna loading in ICRH experiments.

CONCLUSION

We have designed and built a retarding potential analyzer tailored for use in the exhaust of a magnetically confined plasma rocket. By calculating the transmission of the analyzer's collimator over velocity space, we are able to use the collimated RPA as a sensitive diagnostic for the detection and measurement of ion cyclotron heating. Although the ICRH experiments described in this paper were complicated by relatively high background pressure and low coupling of ICRF energy to the plasma, the collimated RPA has found the first unambiguous evidence of ion cyclotron heating in the VX-10 experiment.

---

[1] F. R. Chang-Diaz, Scientific American p. 90 (November, 2000).

[2] R. W. Boswell and F. F. Chen, IEEE Trans. Plasma Sci. **25**, 1229-1244 (1997).

[3] F. F. Chen and R. W. Boswell, IEEE Trans. Plasma Sci. **6**, 1245-1257 (1997).

[4] J. P. Squire et al, Transactions of Fusion Technology **39**, 1 (2002).

[5] B. N. Breizman and A. V. Arefiev, Physics of Plasmas **8**, 907 (2001).

[6] S. Cohen, private communication, November, 2002.

[7] A. Molvik, Rev. Sci. Instrum. **52 (5)**, 704 (1981).

[8] T. S. Green, Plasma Physics **12**, 877 (1970).

[9] S. Stephenakis and W. H. Bennett, Rev. Sci. Instrum. **39**, 1714 (1968).

[10] P. C. Stangeby, *The Plasma Boundary of Magnetic Fusion Devices* (Institute of Physics Publishing, London, 2000), p.90.

[11] R. L. Stenzel, R. Williams, R. Aguero, K. Kitazaki, A. Ling, T. McDonald, and J. Spitzer, Rev. Sci. Instrum. **53 (7)**, 1027 (1982).

[12] R. Krawec, "Effect of an Aperture on Measurement of the Axial Distribution Function

in a Magnetically Confined Plasma", NASA TN D-5746, April, 1970.
[13] E. Y. Wang, J. Appl. Phys. **70**, 2570 (1991).
[14] T. W. Glover, *Measurement of Plasma Parameters in the Exhaust of a Magnetoplasma Rocket by Gridded Energy Analyzer and Emissive Langmuir Probe* , Ph.D. thesis, Rice University, Houston, Texas, 2002.
[15] Y. Okuno, Y. Ohtsu, and H. Fujita, J. Appl. Phys. **74 (10)**, 5990 (1993).